

Stagnation enthalpy effects on turbulent compression corner flow at Mach 5

By M. Di Renzo[†], C. T. Williams, J. Urzay[‡] AND S. Pirozzoli[¶]

The effects of stagnation enthalpy on a Mach-5 boundary layer developing over a compression ramp are analyzed in this work using direct numerical simulations. Two separate sets of simulations, with and without vibrational excitation, are conducted in order to evaluate and isolate stagnation enthalpy effects. It is shown that the variation of the thermodynamic state of the gas can cause 10% variation in skin-friction coefficient, 20% decrease in wall heat flux, and a shift in the typical frequencies of wall pressure fluctuations by a factor of two toward higher frequencies.

1. Introduction

Numerical analyses of high-speed flows have received increasingly more attention over the past few years (Urzay 2018; Candler 2019). Specifically, in hypersonic flows, complex thermochemical effects interact nonlinearly with highly compressible turbulence. Correct predictions of the resulting flow fields are relevant for aerospace engineering problems and pose significant challenges.

One of the main challenges in resolving hypersonic turbulence is the concurrent presence of strong gas-dynamic events, such as shocklets, and wall-bounded turbulence. This interaction makes the numerical prediction of hypersonic turbulence particularly challenging, as low-dissipation and shock-capturing properties are often conflicting features of numerical schemes. The ability to accurately resolve turbulence and stably account for shocks often comes with an increased computational cost. In fact, the increase in available computational resources has only recently allowed investigation of hypersonic turbulent boundary layers (Duan *et al.* 2016; Zhang *et al.* 2018) and compression corners (Priebe & Martin 2021) at low stagnation enthalpies.

Another typical challenge associated with the prediction of hypersonic flows is related to the high enthalpies that are often involved in hypersonic applications. In these flows, the aerodynamic heating generated within the boundary layer leads to a significant increase in gas temperature, whereby vibrational excitation, chemical dissociation, and ionization may be activated (Anderson 2006). These thermochemical phenomena can proceed on timescales that are comparable to those of hydrodynamics, introducing chemical and thermodynamic non-equilibrium. These high-temperature effects have been studied mainly in the context of hypersonic laminar boundary layers, whereas much less is known about their impact on hypersonic turbulent boundary layers (Urzay & Di Renzo 2020; Di Renzo & Urzay 2021; Passiatore *et al.* 2022). Unraveling these phenomena in the context of turbulent compression corners still requires further investigations.

This report presents an analysis of the effects of stagnation enthalpy on a Mach-5

[†] Centre Européen de Recherche et de Formation Avancée en Calcul Scientifique, France

[‡] Presently at US Air Force Research Laboratory

[¶] Sapienza University of Rome, Italy

compression corner flow. Direct numerical simulations (DNS) of a fully turbulent compression corner flow are carried out for different wall-cooling ratios and at two different stagnation enthalpies considering the vibrational excitation of the gas. The rest of the report is organized as follows. Section 2 describes the mathematical and numerical formulation utilized to carry out the presented simulations as well as the computational setup. The main results of the simulations are presented in Section 3, where the analysis is focused mainly on integral quantities of engineering interest, such as the skin-friction coefficient, the heat flux at the wall, and the intensity of the wall pressure fluctuations. Lastly, conclusions are given in Section 4.

2. Formulation and computational setup

The DNS presented in this work have been carried out using the Hypersonic Task-based Research (HTR) solver (Di Renzo *et al.* 2020; Di Renzo & Pirozzoli 2021; Di Renzo 2022). HTR is a compressible Navier–Stokes solver capable of executing large-scale simulations of compressible reacting flows taking into account multicomponent transport and finite-rate chemistry. Specifically, the presented simulations are carried out by solving the conservation equations of mass, momentum, and energy, namely

$$\frac{\partial \rho}{\partial t} + \nabla \cdot (\rho \mathbf{u}) = 0, \quad (2.1)$$

$$\frac{\partial(\rho \mathbf{u})}{\partial t} + \nabla \cdot (\rho \mathbf{u} \mathbf{u}) = -\nabla P + \nabla \cdot \bar{\bar{\tau}}, \quad (2.2)$$

$$\frac{\partial(\rho e_0)}{\partial t} + \nabla \cdot (\rho \mathbf{u} h_0) = \nabla \cdot (\lambda \nabla T + \bar{\bar{\tau}} \mathbf{u}). \quad (2.3)$$

In this formulation, t is the time coordinate, ρ is the density, \mathbf{u} is the velocity vector, P is the thermodynamic pressure, and T is the temperature of the gas. The viscous stress tensor, $\bar{\bar{\tau}}$, is defined as

$$\bar{\bar{\tau}} = \mu \left[\nabla \mathbf{u} + \nabla \mathbf{u}^T - 2(\nabla \cdot \mathbf{u}) \bar{\bar{\mathbf{I}}}/3 \right], \quad (2.4)$$

where $\bar{\bar{\mathbf{I}}}$ is the identity tensor, and the viscosity of the flow is determined as a function of the local temperature using the Sutherland’s law: $\mu = \mu_{ref} (T/T_{ref})^{\frac{3}{2}} (T_{ref} + S) / (T + S)$. In particular, $T_{ref} = 271.15K$ and $S = 110.4K$ have been selected in order to reproduce the behavior of standard air. The formulation is supplemented with the ideal-gas equation of state $P = \rho R_g T$, where R_g is the gas constant.

In Eq. (2.3), $e_0 = e + |\mathbf{u}|^2/2$ and $h_0 = e_0 + P/\rho$ are the specific values of the stagnation internal energy and enthalpy, respectively. In this formulation, e is the specific internal energy that is computed as function of temperature with the expression

$$e = h_r + \int_{T_r}^T c_p dT' - \frac{P}{\rho}, \quad (2.5)$$

where c_p is the constant-pressure specific heat and h_r is a reference enthalpy evaluated at the corresponding temperature T_r .

In this work, two types of gas are considered, using (a) a diatomic calorically perfect gas (CPG) model, for which $T_r = 0$, $h_{ref} = 0$, and $c_p = 7R_g/2$ and (b) a calorically imperfect gas (CIG) with the same value of R_g but whose specific heat capacity and specific enthalpies are computed as functions of the local temperature using the 9-coefficients NASA polynomials particularized for a gas mixture composed of 79% N_2 and 21% O_2 on

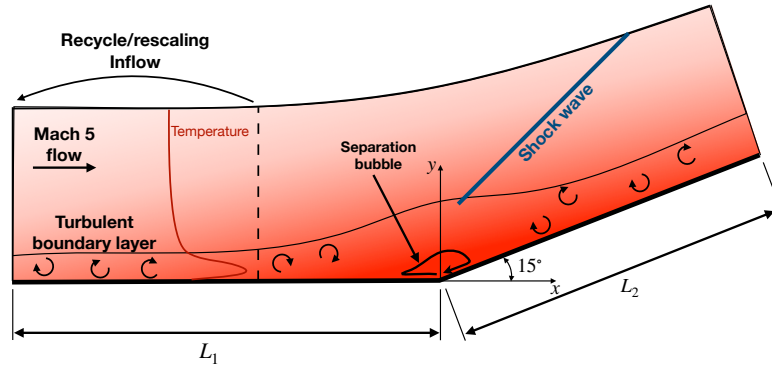


FIGURE 1. Sketch of the computational setup.

a molar basis (McBride *et al.* 2002). In both cases, the thermal conductivity of the gas, λ , is computed as a function of the local viscosity and specific heat capacity at constant pressure with a constant Prandtl number assumption, namely $Pr = c_p \mu / \lambda = 0.71$.

The conservation equations are discretized over a curvilinear computational grid using a conservative formulation (Pirozzoli 2011). In particular, the Euler fluxes are discretized with a sixth-order centered hybrid scheme, whereby a sixth-order skew-symmetric formulation that preserves kinetic energy (Pirozzoli 2010) is utilized in the smooth regions of the flow and a targeted essentially non-oscillatory (TENO) scheme (Fu *et al.* 2016) is used for stencils that are crossed by discontinuities. The smoothness of the flow is measured direction-by-direction using a shock sensor based on the TENO6-A smoothness factors, where the cutoff parameter adaptation is based on a Ducros sensor. The viscous fluxes are discretized in divergence form using a second-order centered scheme. The resulting set of ordinary differential equations is advanced in time using a Runge–Kutta strong-stability-preserving third-order scheme (Gottlieb *et al.* 2001). Further details about the numerical procedures utilized in this work, along with performance analyses of test benchmark cases, can be found in Di Renzo *et al.* (2020).

2.1. Computational setup

The computational setup considered in this study consists of the prismatic domain sketched in Figure 1. A 15° compression corner is located at the origin of the system of coordinates. A Mach-5 turbulent boundary layer of thickness δ_0 is injected through the inflow boundary. The free stream of the incoming boundary layer has a velocity U_e , temperature T_e , and density ρ_e . The distance between the left surface of the domain and the compression corner is equal to $L_1 = 60\delta_0$. The turbulence in the injected boundary layer is sustained using a recycle/rescaling boundary condition (Lund *et al.* 1996), which samples the velocity and temperature fluctuations on a plane located $40\delta_0$ downstream of the inlet plane.

The wall along the compression corner is kept at a constant temperature T_w and is represented by $y_w(x) = d_2 [f(x) - f(-60)]$, where $f(x) = x + \log[\cosh(xd_1)]/d_1$, $d_1 = (1 + d_2^2)^{3/2}/R_c$, and $R_c = 0.05\delta_0$ is the radius of curvature of the compression corner imposed to avoid any discontinuity in the computational grid metrics, while d_2 is numerically determined to guarantee the correct deflection angle.

The top surface of the computational domain is located $10\delta_0$ units above the wall, while its shape is represented by a mathematical expression similar to the bottom wall with

Label	Model	$N_x \times N_y \times N_z$	T_w/T_e	T_{ref}/T_e	h_w/h_{aw}	Re_0	$Re_{\delta_2} _{x=-10\delta_0}$
T22_loH_CPG	CPG	$2560 \times 450 \times 768$	2.2	2.7315	0.400	10^4	1092
T22_hiH_CPG	CPG	$3000 \times 450 \times 1024$	2.2	0.5463	0.400	10^4	1046
T22_hiH_CIG	CIG	$3000 \times 450 \times 1024$	2.2	0.5463	0.354	10^4	1050
T33_loH_CPG	CPG	$2560 \times 256 \times 512$	3.3	2.7315	0.600	1.2×10^4	1190
T33_hiH_CPG	CPG	$2560 \times 256 \times 620$	3.3	0.5463	0.600	1.2×10^4	1132
T33_hiH_CIG	CIG	$2560 \times 256 \times 620$	3.3	0.5463	0.625	1.2×10^4	1132

TABLE 1. Characteristic parameters of the presented simulations where N_x , N_y , and N_z are the number of grid points along the Cartesian directions, $Re_0 = \rho_e u_e \delta_0 / \mu_e$ is the Reynolds number computed at the inlet with the edge conditions, and $Re_{\delta_2} = \rho_e U_e \theta / \mu_w$ is the Reynolds number based on the momentum thickness θ and the viscosity at the wall.

$R_c = 10\delta_0$. The boundary condition along the top surface is treated with a characteristic far-field boundary condition that switches between a characteristics-based outflow (if the local flow exits the surface) and a non-reflective inflow that weakly imposes the free-stream conditions (if the flow locally enters the domain).

The right surface of the computational domain is positioned $L_2 = 40\delta_0$ downstream of the compression corner and is modeled using a non-reflective outflow (Poinsot & Lele 1992). The computational domain is $10\delta_0$ wide in the z direction normal to the sketch, along which periodicity is enforced.

The computational grid is uniform along the periodic direction and is stretched with a hyperbolic sine function in the wall-normal direction to achieve a grid spacing that is smaller than unity in local friction (plus) units for the entire computational domain. Approximately 30% of the grid points assigned to the streamwise direction are uniformly distributed in the region of the computational domain upstream of the interaction, whereas the rest of the points are smoothly clustered downstream of the compression corner using a sigmoid function in order to achieve a uniform grid resolution normalized in local friction units.

The results shown below correspond to six cases, whose main parameters are summarized in Table 1. The subscripts e and w mean that the quantity is evaluated at the edge of the incoming boundary layer and at the wall, respectively. These simulations differ mainly with respect to the thermodynamic state of the free stream, the dimensionless temperature of the wall, and the thermodynamic model that describes the gas. The simulations with $T_{ref}/T_e = 2.7315$ are at low-enthalpy conditions ($T_e = 100K$) and are representative of the state of the art for DNS of hypersonic compression ramps. The setups at $T_{ref}/T_e = 0.5463$ ($T_e = 500K$) have higher stagnation enthalpy, and they reach thermodynamic states that activate vibrational excitation within the boundary layer. For this reason, these simulations are carried out both with the CPG and CIG models. In this way, the influence of the variation of the viscosity field on the flow is highlighted by comparing the high- and low-enthalpy CPG simulations, whereas the effects of vibrational excitation are observed while comparing the two high-enthalpy simulations with different thermodynamic models. Moreover, two different wall temperatures are analyzed to define the effects of wall cooling on the flow. Note that for the CIG simulations, the ratio h_w/h_{aw} changes nonlinearly with the wall temperature. In fact, while the adiabatic wall enthalpy, $h_{aw} = h_e + ru_e^2/2$, is constant regardless of the thermodynamic model, h_w is a nonlinear function of the wall temperature for the CIG. For this reason, the ratio h_w/h_{aw} in CIG is lower/higher than the corresponding CPG cases for the higher/lower wall temperature. In the adiabatic-wall-enthalpy expression, $r = 0.9$ is the recovery fac-

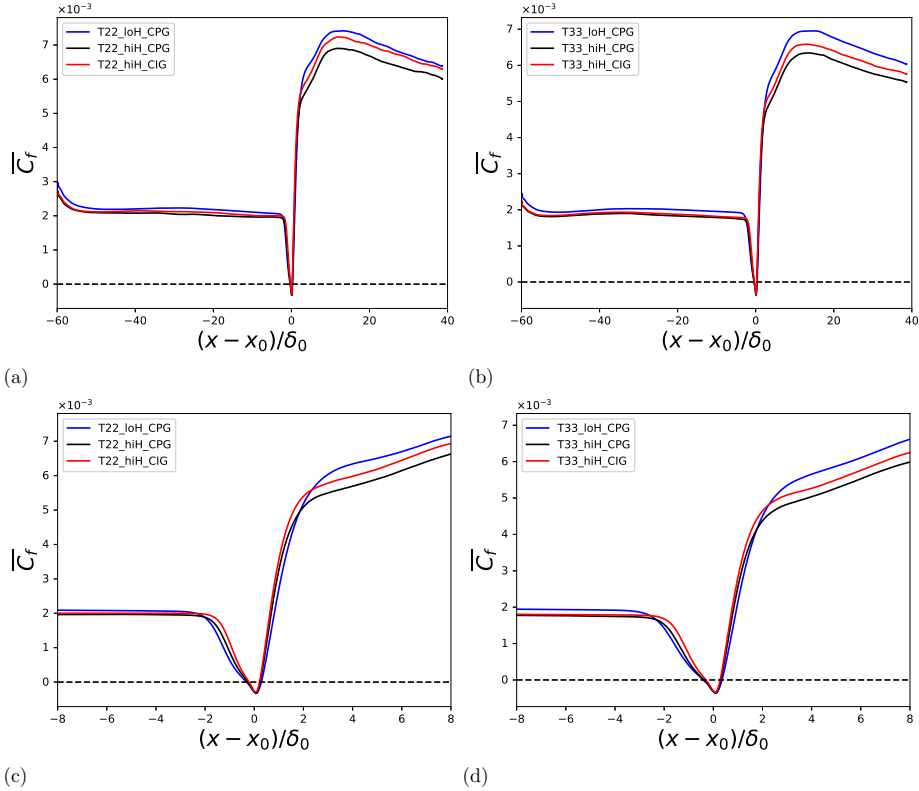


FIGURE 2. Skin-friction coefficient as a function of streamwise distance for (a) $T_w/T_e = 2.2$ and (b) $T_w/T_e = 3.3$. Panels (c) and (d) are analogous to (a) and (b), respectively, but they show a zoomed-in version of the results near the compression corner.

tor that here is assumed to be constant regardless of the thermodynamic state of the gas.

3. Results

The numerical results presented in this section are collected after 10 flow residence times based on the edge velocity and the length of the computational domain. Statistics are computed for an additional 10 flow residence times for convergence. In the formulation employed below, the overline symbol indicates a Reynolds average, or equivalently, an unweighted average along both time and the spanwise direction.

3.1. Skin-friction coefficient and wall heat flux

Figure 2 shows the distributions of the skin-friction coefficient $C_f = 2\tau_{nt}/(\rho_e U_e^2)$ with $\tau_{nt} = \overline{\hat{\tau}}\hat{n}\hat{t}$, where \hat{n} and \hat{t} are the versors normal and tangential to the wall, respectively. All the analyzed boundary layers require an adaptation length of about $20\delta_0$ downstream of the inflow. At this location, which corresponds to the inflection point in the C_f profile, the boundary-layer turbulence achieves a physically meaningful state that is not affected by the recycle/rescaling boundary condition. A small recirculation bubble of approximate size δ_0 is generated as a result of shock-wave/boundary-layer interaction (SBLI) at the compression corner. As observed in Figure 2(a,b), an overall trend in the cases involving

CPG away from the separation and reattachment zones is a 10% decrease in the skin-friction coefficient upon increasing the stagnation enthalpy by 400%. However, an increase in the skin-friction coefficient is observed when swapping the assumption of CPG for the CIG approximation. As a result, the aforementioned increase in stagnation enthalpy leads to only a moderate decrease of approximately 5% in the skin-friction coefficient when vibrational-excitation effects are incorporated. Additionally, an increase in wall temperature leads to an overall decrease in the skin-friction coefficient. In contrast, as shown in Figure 2(c,d), the size of the separation bubble appears to remain mostly unaltered across all cases.

A variation of the stagnation enthalpy modifies significantly the flow just upstream of the separation bubble, although the bubbles themselves remain largely unaffected by the change in the thermodynamic model. In particular, the departure from the classical C_f scaling is delayed by the increase in the stagnation enthalpy and by the introduction of the CIG model. These differences observed between the low- and high-enthalpy setups are to be attributed to Reynolds number effects. In fact, the two CPG simulations differ only in the relation between the molecular viscosity and the local temperature. The lower enthalpy conditions experience a larger variation of viscosity across the boundary layer, leading to lower local Reynolds numbers. The additional endothermicity introduced by the CIG model reduces the amplitude of the temperature peak generated in the boundary layer, thus decreasing the maximum viscosity of the fluid and further increasing the local Reynolds number. As higher Reynolds number flows are less prone to separate and the separation bubble is located across the compression corner, the C_f profile of the higher Reynolds flow, therefore, has a steeper transition. For this reason, the increase in the stagnation enthalpy and the introduction of the CIG model steepen the C_f profiles upstream of the separation point.

Figure 3 shows the distribution of the wall heat flux using two different normalizations. The first is the classic Stanton number, defined as $St = q_w / [\rho_e U_e (h_{aw} - h_w)]$, where q_w is the heat flux at the wall. The second normalization is based on the free-stream momentum flux, namely $C_q = q_w / (\rho_e U_e^3)$, as proposed by White (1992) specifically for hypersonic flows of CIG. Interestingly, the behavior of the normalized heat flux depends strongly on the chosen normalization, as a consequence of the nonlinear relationship between enthalpy and temperature in CIG. If the Stanton number distribution is considered, the effects of vibrational excitation are very similar to those observed in the skin-friction coefficient. Specifically, the highest Stanton number is found in the low-enthalpy case, whereas the high-enthalpy CPG case shows a reduction of about 10%. The CIG simulations lie in between the two CPG simulations for both wall-cooling intensities considered in this study. These results show that the Reynolds analogy ($C_f/St \sim 2$) is approximately preserved in CPG and CIG setups.

If the heat-flux coefficients are considered instead, a new interpretation of the CIG effects presents itself. In particular, the red curve is shifted downward in Figure 3(c,d). This is the effect of the endothermicity induced by vibrational excitation. The variation of the heat capacity lowers the temperature peak arising because of viscous heating. As a result, the temperature gradients and the wall heat flux are milder. This second normalization emphasizes the reduction in the temperature gradient by vibrational excitation because the normalizing factor $\rho_e U_e^2$ is constant for the high-enthalpy CPG and CIG setups. We believe that this ambiguity in interpreting the results prompts further studies regarding the most appropriate normalization of heat fluxes in boundary layers of CIG.

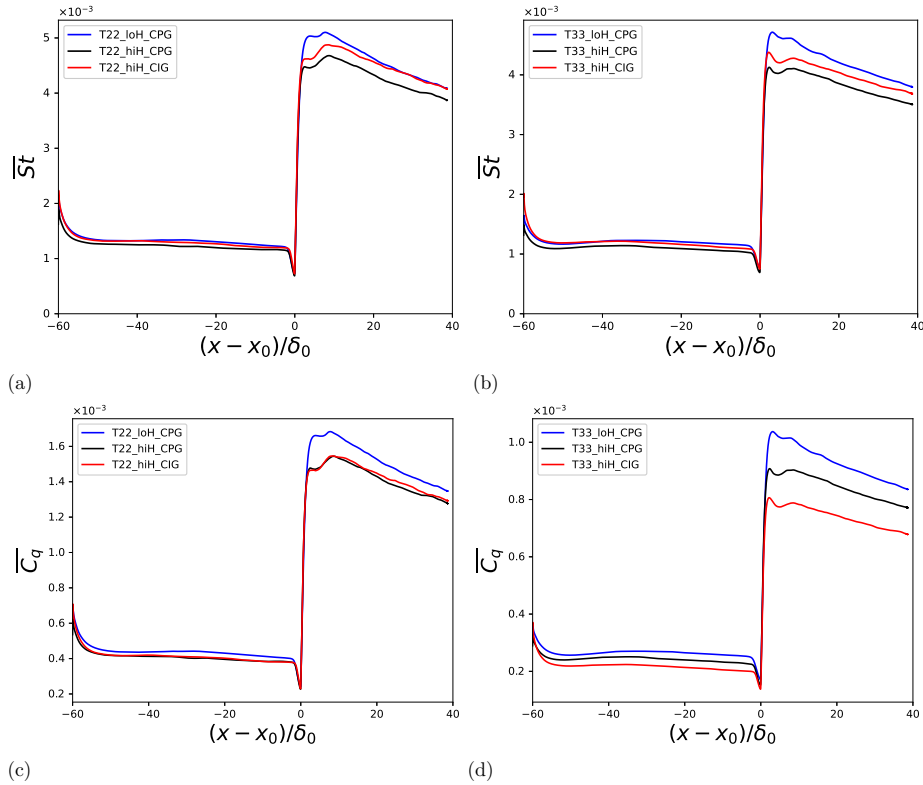


FIGURE 3. Streamwise distributions of (a,b) Stanton number and (c,d) wall-heat-flux coefficient for flow cases with (a,c) $T_w/T_e = 2.2$ and (b,d) $T_w/T_e = 3.3$.

3.2. Wall pressure fluctuations

Figure 4 shows the main statistics and the spectral properties of wall pressure fluctuations induced by the SBLI for the six computational setups, along with an instantaneous density field. The root-mean-squared pressure fluctuation profiles are shown in Figures 4(a,b). The fluctuation intensity is about 10% of the pre-shock mean free-stream pressure, up to a distance $2\delta_0$ from the compression corner. Past this location, the pressure fluctuation intensity rises, showing the upstream influence of the SBLI that is generated at the compression corner. The distributions feature a second kink around the compression corner, where the growth of the pressure fluctuations becomes steeper for an additional distance $2\delta_0$. The maximum of the pressure fluctuations intensity is then achieved about $5\delta_0$ downstream of the compression corner. The effects of the thermodynamic conditions of the gas on this peak are very similar to those observed for the skin-friction coefficient. The low-enthalpy case shows the strongest pressure fluctuations, the high-enthalpy CPG setup has the weakest pressure fluctuations, and the high-enthalpy CIG case lies in between. The peak pressure fluctuations intensity is usually located at the shock foot in supersonic SBLIs, as the shock motion induces large footprints in terms of wall pressure. One of the most interesting aspects of the present results is that the strongest pressure fluctuations are not generated by the shock itself. In fact, the peak of pressure fluctuations occurs where the large eddies generated in the outer portion of the upstream boundary layer impinge on the shock wave and the ramp following the compression corner, as shown

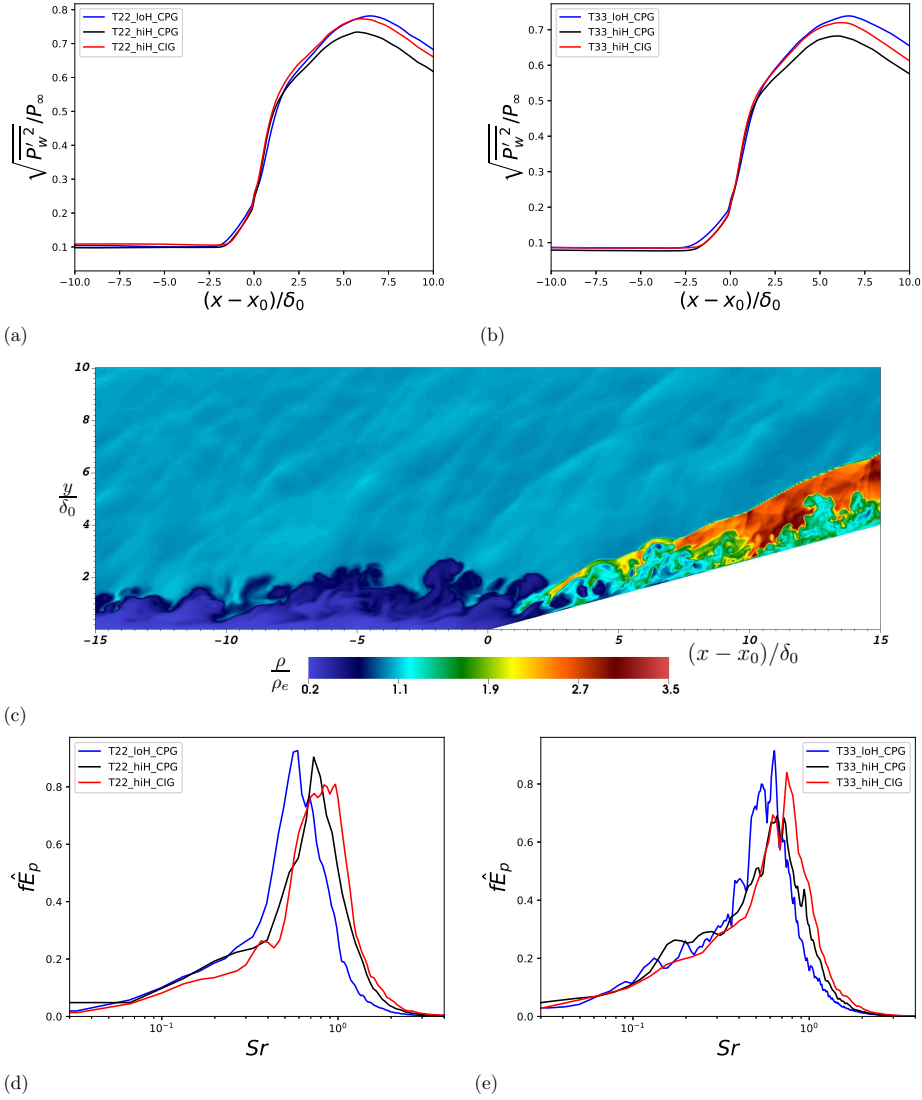


FIGURE 4. (a,b) Streamwise distribution of root-mean-square wall pressure. (c) Instantaneous contours of density in the x - y plane for the case T22_loH_CPG. (d,e) Premultiplied power spectrum of pressure fluctuations at the compression corner. Panels (a,c,d) and (b,e) refer to the cases with $T_w/T_e = 2.2$ and $T_w/T_e = 3.3$, respectively.

in the instantaneous density contours in Figure 4(c). These highly energetic structures are able to severely corrugate and sometimes disrupt the surface of the shock wave, thus generating a highly intermittent pressure field.

The premultiplied spectra of the wall pressure signal extracted at the compression corner location, shown in Figures 4(a,b), demonstrate that the free-stream stagnation enthalpy is capable of modifying the spectral properties of the wall pressure fluctuations. The reported spectra do not show a significant energy content in the low-wave number range of the spectrum, as the interaction is relatively weak. On the other hand, the energy is localized mostly at Strouhal number $Sr = f\delta_0/U_e \sim 1$, where f is the signal frequency,

for all the simulations presented in this report. This range of frequencies is typical of wall turbulence and suggests that the analyzed wall pressure fluctuations are due mainly to the incoming boundary layer. The increase in the stagnation enthalpy of the flow and the introduction of vibrational excitation have the effect of shifting the energy peak toward higher frequencies as a consequence of the local Reynolds number variations discussed in Section 3.1.

4. Conclusions

We have carried out DNS of Mach-5 turbulent boundary layers flowing over a 15° compression ramp. Two rates of wall cooling and two levels of stagnation enthalpy have been considered. The lowest stagnation enthalpy is representative of the state of the art of hypersonic turbulence simulations, and it considers a flow with a free-stream temperature of $100K$ that remains in the CPG regime throughout the computational domain. The highest stagnation enthalpy corresponds to a free-stream temperature of $500K$, which is sufficiently high to allow the gas molecules to become vibrationally excited within the turbulent boundary layer formed over the compression ramp and across the ramp-induced shock wave. However, the maximum gas temperature encountered in all these cases always remains lower than $2000K$, which warrants marginal activation of other high-temperature effects, such as chemical dissociation.

Increasing the stagnation enthalpy of the flow while retaining the CPG assumption decreases the skin-friction coefficient, the Stanton number, and the wall pressure fluctuations by about 10%. Introduction of endothermic effects associated with vibrational excitation partially compensates for this decrease, yielding values of the normalized mechanical and thermal stresses at the wall that are halfway between the low-enthalpy and high-enthalpy calorically perfect flow solutions. However, a different normalization of the heat flux, which does not take into account the nonlinear relation that exists between temperature and enthalpy in the CIG model, shows that vibrational excitation actually decreases the heat flux at the wall by about 20%. The conflicting conclusions offered by two normalizations prompt for further investigation into the correct scaling for this quantity. Another effect associated with stagnation enthalpy variation which has some engineering relevance is the shift of the wall pressure fluctuations toward higher frequencies. In fact, the increase in stagnation enthalpy in the CPG simulation and the introduction of vibrational excitation increase the peak frequency of pressure fluctuations at the compression corner. Considering that the most energetic frequency shifts by a factor of two between the low-enthalpy and high-enthalpy vibrationally excited flow, it appears that high-enthalpy effects should be taken into account when dynamical loads generated by this type of flow are evaluated.

The results reported in this study provide an initial assessment of the importance of high-enthalpy effects in the prediction of hypersonic wall-bounded turbulence and, in particular, of hypersonic shock-wave/turbulent-boundary-layer interactions. However, the flow conditions under scrutiny here are at the lower end of the hypersonic regime, and the free-stream enthalpy is such that only vibrational excitation is triggered. Future work will focus on verifying the conclusions of this study for flows at higher Mach numbers and higher enthalpy, in which chemical and thermal non-equilibrium effects play a role.

Acknowledgments

MDR and SP are grateful to the CTR Steering Committee for selecting this project for the 2022 Summer Program. These simulations utilized computational resources provided

by the US Department of Energy's National Nuclear Security Administration, Grant # DE-NA0003968, as part of the PSAAP-III (INSIEME) Center at Stanford University.

REFERENCES

- ANDERSON, J. D., JR. 2006 *Hypersonic and High-Temperature Gas Dynamics*, AIAA.
- CANDLER, G. V. 2019 Rate effects in hypersonic flows. *Annu. Rev. Fluid Mech.* **51**, 379–402.
- DI RENZO, M. 2022 HTR-1.3 solver: Predicting electrified combustion using the Hypersonic Task-based Research solver. *Comput. Phys. Commun.* **272**, 108247.
- DI RENZO, M., FU, L. & URZAY, J. 2020 HTR solver: An open-source exascale-oriented task-based multi-GPU high-order code for hypersonic aerothermodynamics. *Comput. Phys. Commun.* **255**, 107262.
- DI RENZO, M. & PIROZZOLI, S. 2021 HTR-1.2 solver: Hypersonic Task-based Research solver version 1.2. *Comput. Phys. Commun.* **261**, 107733.
- DI RENZO, M. & URZAY, J. 2021 Direct numerical simulation of a hypersonic transitional boundary layer at suborbital enthalpies. *J. Fluid Mech.* **912**, A29.
- DUAN, L., CHOUDHARI, M. M. & ZHANG, C. 2016 Pressure fluctuations induced by a hypersonic turbulent boundary layer. *J. Fluid Mech.* **804**, 578–607.
- FU, L., HU, X. Y. & ADAMS, N. A. 2016 A family of high-order targeted ENO schemes for compressible-fluid simulations. *J. Comput. Phys.* **305**, 333–359.
- GOTTLIEB, S., SHU, C.-W. & TADMOR, E. 2001 Strong stability-preserving high-order time discretization methods. *SIAM Review* **43**, 89–112.
- LUND, T. S., WU, X. & SQUIRES, K. D. 1996 On the generation of turbulent inflow conditions for boundary layer simulations. *J. Comput. Phys.* **140**, 233–258.
- MCBRIDE, B. J., ZEHE, M. J. & GORDON, S. 2002 NASA Glenn coefficients for calculating thermodynamic properties of individual species. NASA/TP, 211556.
- PASSIATORE, D., SCIACOVELLI, L., CINNELLA, P. & PASCAZIO, G. 2022 Thermochemical non-equilibrium effects in turbulent hypersonic boundary layers. *J. Fluid Mech.* **941**, A21.
- PIROZZOLI, S. 2010 Generalized conservative approximations of split convective derivative operators. *J. Comput. Phys.* **229**, 7180–7190.
- PIROZZOLI, S. 2011 Stabilized non-dissipative approximations of Euler equations in generalized curvilinear coordinates. *J. Comput. Phys.* **230**, 2997–3014.
- POINSOT, T. J. & LELE, S. K. 1992 Boundary conditions for direct simulations of compressible viscous flows. *J. Comput. Phys.* **101**, 104–129.
- PRIEBE, S. & MARTIN, M. P. 2021 Turbulence in a hypersonic compression ramp flow. *Phys. Rev. Fluids* **6**, 34601.
- URZAY, J. 2018 Supersonic combustion in air-breathing propulsion systems for hypersonic flight. *Annu. Rev. Fluid Mech.* **50**, 593–627.
- URZAY, J. & DI RENZO, M. 2020 Engineering aspects of hypersonic turbulent flows at suborbital enthalpies. *Annual Research Briefs*, Center for Turbulence Research, Stanford University, pp. 7–32.
- WHITE, F. M. 1992 *Viscous Fluid Flow*, McGraw-Hill.
- ZHANG, C., DUAN, L. & CHOUDHARI, M. M. 2018 Direct numerical simulation database for supersonic and hypersonic turbulent boundary layers. *AIAA J.* **56**, 4297–4311.